aptamer candidates displayed on the particles are then incubated with fluorescently-labeled target, and the fluorescence intensity of each particle is measured using FACS. These intensities enable quantitative determination of aptamer affinity and the effective separation of weak and strong binders. Finally, the sorted high-affinity aptamer particles are directly amplified by PCR, and this enriched pool of aptamer candidates is used in the next selection round. Prior to particle display screening, we performed two rounds of conventional selection with a pool of 10^{14} randomized library molecules using S protein-immobilized magnetic beads, because the FACS instrument has a practical throughput limitation of 4×10^7 particles per h. We then used this pre-selected pool for particle display screening with an initial library of 10^8 aptamer particles. Four rounds (R1–R4) of screening were performed by reducing the target concentration in a stepwise manner from 10 nM to 2 nM (Fig. 2A). We set the sort gate to collect 0.1–0.2% of the top binder population with the strongest fluorescence signals in the FACS dot plot (Fig. 2A, blue box). As a control, the fluorescence intensity of forward primer (FP)-coated particles with no aptamer expressed was measured in order to calibrate the "reference gate" for non-binders in the FACS screen (Fig. 2A, black box). In R1, to avoid losing high-affinity aptamer candidates, we began selection with a low screening stringency by setting a wide sort gate. The isolated aptamer candidates were then amplified by PCR to synthesize the aptamer particles for the next round. In subsequent rounds, we further narrowed the sort gate thresholds to increase the screening stringency. After R2, the population shift of the red fluorescence signal was greatly increased, indicating that high-affinity aptamer candidates were being enriched (Fig. 2B). By R4, there was no further population shift in terms of fluorescence, and we therefore determined that we had achieved peak enrichment and stopped screening in order to perform sequencing analysis of the enriched pool.

We initially tried to isolate the top binders from R4 based on binding to 2 nM S protein, but this yielded an excessively large population with strong red fluorescence. Unlike in other rounds, there were two large populations represented within the reference gate in the R4 pool, one of which appeared to be budding off from the other (Fig. 2A). To investigate whether the best aptamer sequence belonged to a large population with moderate fluorescence intensities in this 'budding' population or the sort-gated population with the highest fluorescence intensities, we sorted out the different populations at different concentrations (Fig. 2C). The sort gates were set separately into groups of 0.15% top binders and 5% top binders, respectively, of round 4 sorting at 2 nM concentration. In addition, a separate sorting experiment was performed that collected 0.1% of top binders of the same round 4 pool at 0.5 nM as the optimal concentration of S protein based on the result of the extra binding assay.

3.2. Selection of a high-affinity S protein-binding DNA aptamer

We then performed bacterial cloning and Sanger sequencing of R4 sorted DNA aptamer candidates. Our sequencing analysis revealed four different consensus sequences. Two of these, SpS1-C1 and C2, were respectively observed among the 0.15% and 5% top binders from the 2

nM S protein sorting condition, whereas the other two groups (SpS1-C3 and -C4) were only observed in the top binders from the 0.5 nM S protein extra sorting experiment (Table 1). These aptamer candidates were individually synthesized as monoclonal aptamer particles via PCR amplification on forward primer-coated magnetic beads. Next, a binding assay was performed with each monoclonal aptamer particle to find the best S protein aptamer candidate via FACS analysis. The results showed that SpS1-C1 and SpS1-C4 clearly exhibited the greatest target affinity (Fig. 3A). And then, the specificity test was conducted on the receptor-binding domain (RBD), subunit 1 (S1), and subunit 2 (S2) domain of the S protein to confirm the aptamer binding sites, with BSA as a control. These results indicate that both aptamers specifically bind to S1 domain of the S protein (Fig. 3B). Finally, the binding affinity of the two aptamers was determined using fluorescently-labeled S protein trimers through a bead-based fluorescence binding assay (Ahmad et al., 2011). The binding data were evaluated using GraphPad software with a 1:1 binding model to determine the dissociation constant (Kd) values (Fig. 3C and D). The two aptamers exhibited excellent affinity, with Kd values of 1.47 ± 0.30 nM and 1.81 ± 0.39 nM for SpS1-C1 and -C4, respectively.

3.3. A label-free SERS-based DNA aptasensor for ultra-sensitive detection of S protein

We then designed a label-free, SERS-based aptasensor using these newly generated DNA aptamers. To achieve effective enhancement of Raman signals, we fabricated a three-dimensional nanostructured silver nanoforest (SNF) substrate (Kim et al., 2021) using the nano-sputtering method (Fig. 4A), followed by conjugation of the two spike-binding aptamers onto the surface of the SNF substrate. Further, it is widely accepted that silver nanoparticles exhibit higher SERS enhancement than gold nanoparticles (Zhao et al., 2008). We also were able to observe the intrinsic signal of DNA aptamer on the SNF substrate. This intrinsic signal-based aptasensor enables detection without the need for incorporation of any Raman labels.

First, the morphology of the SNF substrate was verified via scanning electron microscopic (SEM) analysis (Fig. 4B). This revealed a silver nanoporous structure with a thickness of approximately 1.2 μm; for reference, the original silver nanoparticles were approximately 75 nm in diameter. This three-dimensional nanostructure should be capable of effectively amplifying Raman signals. To verify the suitability of the SNF substrate, the SERS signals were measured, which were produced by droplets of a solution containing various concentrations of rhodamine 6G (R6G) solution, a well-known Raman tag (Fig. 4C). We confirmed the presence of the R6G-specific peak at 1,511 cm^{-1}, which is the product of aromatic C–C stretching vibrations (Pang et al., 2014). We subsequently plotted the Raman intensity at 1,511 cm^{-1} relative to the concentration of R6G, and confirmed that as the R6G concentration decreased, the magnitude of this peak also decreased (Fig. 4D). Based on this analysis, we determined a detection limit of 2×10^{-12} mol. In order to confirm the usability of the SNF substrate as a SERS substrate, the reproducibility

Table 1
Consensus sequences from the R4 aptamer pool.

| Aptamer ID	Sequence (5′–3′)	Length	Sorting Condition
SpS1-C1	GAACATTGGCGTCCGTGAG-TGAGACCATAGTCCAGCGAACTAAACCTACCCTAAAGGGCAAGGAAGACGGG-CACTTCCTCAAACGCCCAA	90mer	0.15%@2 nM
SpS1-C2	GAACATTGGCGTCCGTGAG-CTGCAATATCTTCTTCAATGCCCTGCTGCCACCACTGGCTTCACTTGCGTGT-CACTTCCTCAAACGCCCAA	90mer	5.0%@2 nM
SpS1-C3	GAACATTGGCGTCCGTGAG-AGATTATAATCCATCTGACGAGTTGTTTTACCGATATTTATCAGTTTTTGTT-CACTTCCTCAAACGCCCAA	90mer	0.1%@0.5 nM
SpS1-C4	GAACATTGGCGTCCGTGAG-CAGCTCGTGGTTGTTTGCTTGTATACTTTTGTGGTTTATCTTGTTTCTGAT-CACTTCCTCAAACGCCCAA	89mer	0.1%@0.5 nM
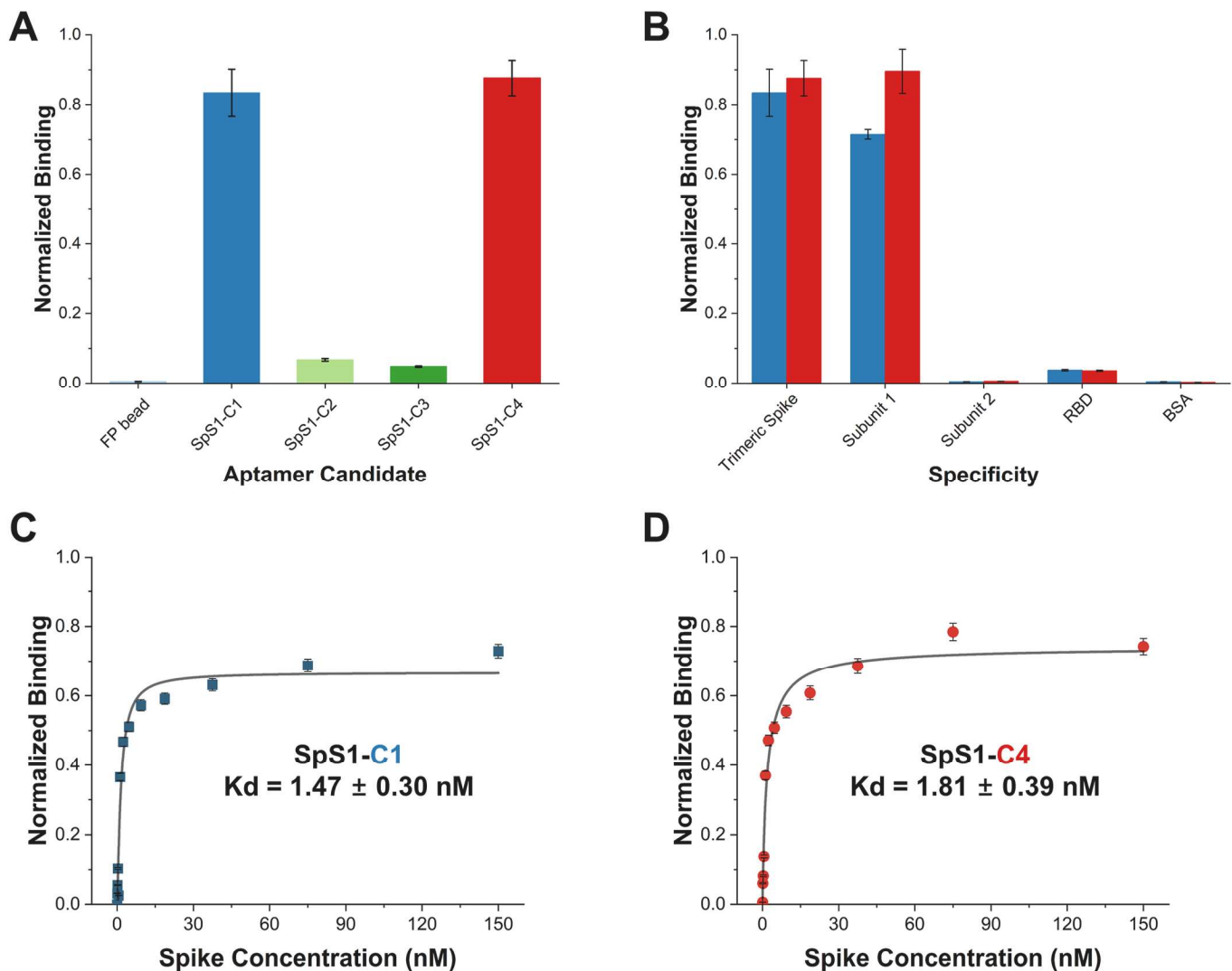
Fig. 3. Characterization of the isolated S protein-binding aptamers. (A) Candidate aptamers from each of the four consensus sequence families were chosen for further analysis. 'FP bead' indicates the forward primer-coated bead used as a negative control. (B) Specificity measurements were also conducted against the trimeric S protein, subunit 1, subunit 2, the receptor-binding domain (RBD), and bovine serum albumin (BSA). (C, D) Dissociation constant (Kd) measurements of the best aptamers using a bead-based fluorescence assay. Kd was calculated from the fluorescence intensity of binding in a 1:1 binding model using GraphPad software.

and anti-interference capability of the SNF substrate were confirmed (Fig. S4 and Fig. S5). The reproducibility of SNF substrate was analyzed through Raman signal measurement of R6G with a concentration of 1 mM for 20 different SNF substrates, and the error range was about 6.67%. In addition, the anti-interference capability of the SNF substrate was confirmed using a mixture of R6G and Nile blue A, and it was confirmed that the characteristic peak (599 cm^{-1}) of Nile Blue A was well measured in this mixture. Furthermore, Fourier transform infra-red (FTIR) analysis was also conducted (Fig. S6). It was observed that no peak occurred on the bare SNF substrate. In comparison, the aptamer-conjugated SNF showed that two peaks of 1,429 cm^{-1} and 2, 962 cm^{-1} caused by O–H bending of carboxyl acid and C–H stretching of alkanes, respectively. In addition, X-ray diffraction (XRD) patterns were also analyzed for bare SNF substrate and aptamer conjugated SNF substrate (Fig. S7). XRD peaks at 2θ of 38.18°, 44.25°, 64.72°, and 77.40° could be attributed to the (111), (200), (220), and (311) crystallographic planes of the face-centered cubic silver crystals, respectively. Therefore, the XRD pattern clearly demonstrated that Ag-based nanostructures were formed in this research. The main crystalline phase was silver, and there were no obvious other phases, such as impurities, found in the XRD patterns. Finally, the long-term stability of aptasensor over 5

days was also confirmed (Fig. S8). The intensities at 1,587 cm^{-1} were barely changed. From these results, we were able to successfully form a nanoscale gap, and using this, we manufactured an SNF substrate, which was confirmed to be available as a SERS substrate. The nanoscale gap used here formed a strong hot spot by forming a three-dimensional nanoporous structure, which is thought to have amplified the Raman signal of the sample.

We then conjugated SpS1-C1 and -C4 aptamers onto the surface of the SNF substrate. These aptamers were modified with a thiol group at the 5′-end to ensure consistent orientation after immobilization, which could in turn enhance binding affinity (Abdelhamid et al., 2022). We first recorded the intrinsic Raman signals of the conjugated aptamers on the SNF surface (Fig. 4E–G). We observed a strong Raman signal in the 1, 400–1,600 cm^{-1} spectral range, corresponding to the vibrations of ketones and some guanine deformation (Gillibert et al., 2018). We also saw several additional peaks, including a 768 cm^{-1} peak corresponding to the C–C and C–N stretching of adenine and thymine (Barhoumi and Halas, 2010) and a 1,317 cm^{-1} peak produced by the N–C of adenine and guanine (Gao et al., 2017) (Fig. S9). Next, we added the recombinant trimeric S protein to the aptamer-conjugated SNF substrate at varying concentrations. The Raman signals of the two aptamers were
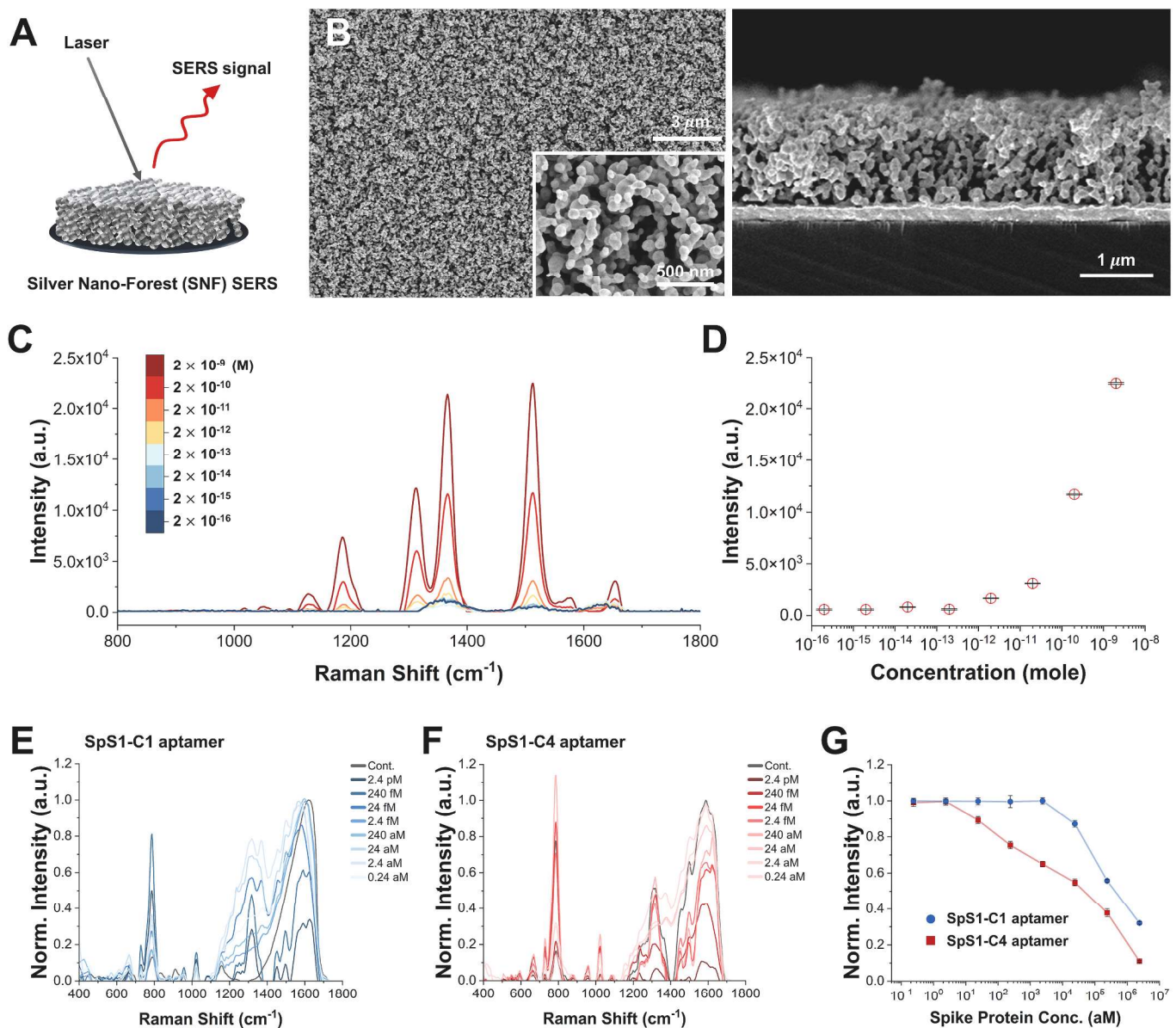
Fig. 4. Design of the label-free SERS-based aptasensor. (A) Schematic illustration of SERS analysis using the SNF substrate. (B) Top and side view scanning electron microscopy (SEM) images of the SNF substrate. (C) Raman spectra with varying concentrations of rhodamine 6G on the SNF substrate. (D) Concentration-dependent Raman intensity of rhodamine 6G at 1,511 cm^{-1}. (E–G) Raman shifts of intrinsic signals for (E) SpS1-C1 and (F) SpS1-C4 at varying concentrations of the recombinant trimeric S protein. (G) The data show the detection limit of SpS1-C1 and -C4 on the SNF substrate based on Raman signal intensity at 1,587 cm^{-1}.

considerably altered at the highest concentration of S protein (10 ng/mL), and as the protein concentration decreased, the Raman signal changes also decreased. At low concentrations such as 1 or 10 pg/mL, the Raman signal was virtually unchanged relative to before protein administration. To further quantify this concentration-dependent response, we focused specifically on the above-mentioned peaks in Raman intensity at positions 768, 1,317, and 1,587 cm^{-1}. We chose the Raman signal at 1,587 cm^{-1} with the most prominent signals and the smallest experimental error compared to the other two positions (768 and 1,317 cm^{-1}) (Fig. 4E–G and Fig. S9). We confirmed a detection limit of 240 fM and 240 aM for aptamers SpS1-C1 and -C4, respectively, using 1,587 cm^{-1} Raman signals (Fig. 4G). The reasons why the Raman signal is decreasing are as follows. The 3′ part of the aptamer strand is close to the SNF surface before the SARS-CoV-2 S protein binds. After binding, a 3D structure consisting of an aptamer-protein complex is formed, which is expected to decrease the Raman signal as the 3′ part of the aptamer moves away from the SNF surface. These results confirmed that the SNF

substrate can be used as an effective SERS substrate and that this aptasensor is the most sensitive for the detection of the SARS-CoV-2 S protein when we employ our best aptamer (Fig. 4G and Table S2).

3.4. Clinical validation of our SERS aptasensor for multiple SARS-CoV-2 variants

Since the initial discovery of SARS-CoV-2 in 2019, the ancestral Wuhan wild-type strain has given rise to a host of variants with altered transmissibility, pathogenicity, and potential for immune escape, including the Alpha (B.1.1.7), Beta (B.1.351), Gamma (P.1), Epsilon (B.1.429), Delta (B.1.617.2), and Omicron (B.1.1.529) variants. Although various commercial RATs have been developed for these, several of these have proven incapable of detecting the now-widespread Omicron variant, even days after the infection (Adamson et al., 2022). This remains a serious problem for managing the spread of COVID-19, and given that this virus still has abundant opportunities for the

emergence of novel lineages, there is a clear need for diagnostic tools capable of detecting a broad range of variants.

We, therefore, validated the utility of our aptasensor platform using SpS1-C4 for testing actual clinical samples collected from patients with COVID-19 (Fig. 5 and Figs. S10–S13). Considering the improved accuracy, SpS1-C4 was chosen to validate clinical samples because it is 1000-fold more sensitive than the SpS1-C1 aptamer. We used 80 clinical nasopharyngeal samples obtained from the Sejong Institute of Health & Environment: 20 known negatives, and 20 samples each from known positives with wild-type, Delta, and Omicron variants. The results were verified by RT-qPCR (Table S3). In the negative samples, there was no binding with the target, and thus only a negligible difference in Raman

signals at 1,587 cm^{-1}. In contrast, we consistently observed a dramatic decrease in Raman signals with all 60 COVID-19 positive samples (Fig. 5A–D and Figs. S10–S13). Using these data, we conducted a receiver operating characteristic (ROC) curve analysis to assess the sensitivity and specificity of the platform. Based on ROC analysis, we determined the decision threshold to be an intensity ratio of 0.5575 (Fig. 5E). The decision threshold was determined as the average between the sum of negative values and the sum of positive values of Wild-type, Delta, and Omicron in Fig. 5E. Only one sample showed a false negative (WT-15), and this was subsequently attributed to failed conjugation of the aptamer onto the SNF substrate, based on the absence of intrinsic Raman signals from the aptamer. The area under the curve
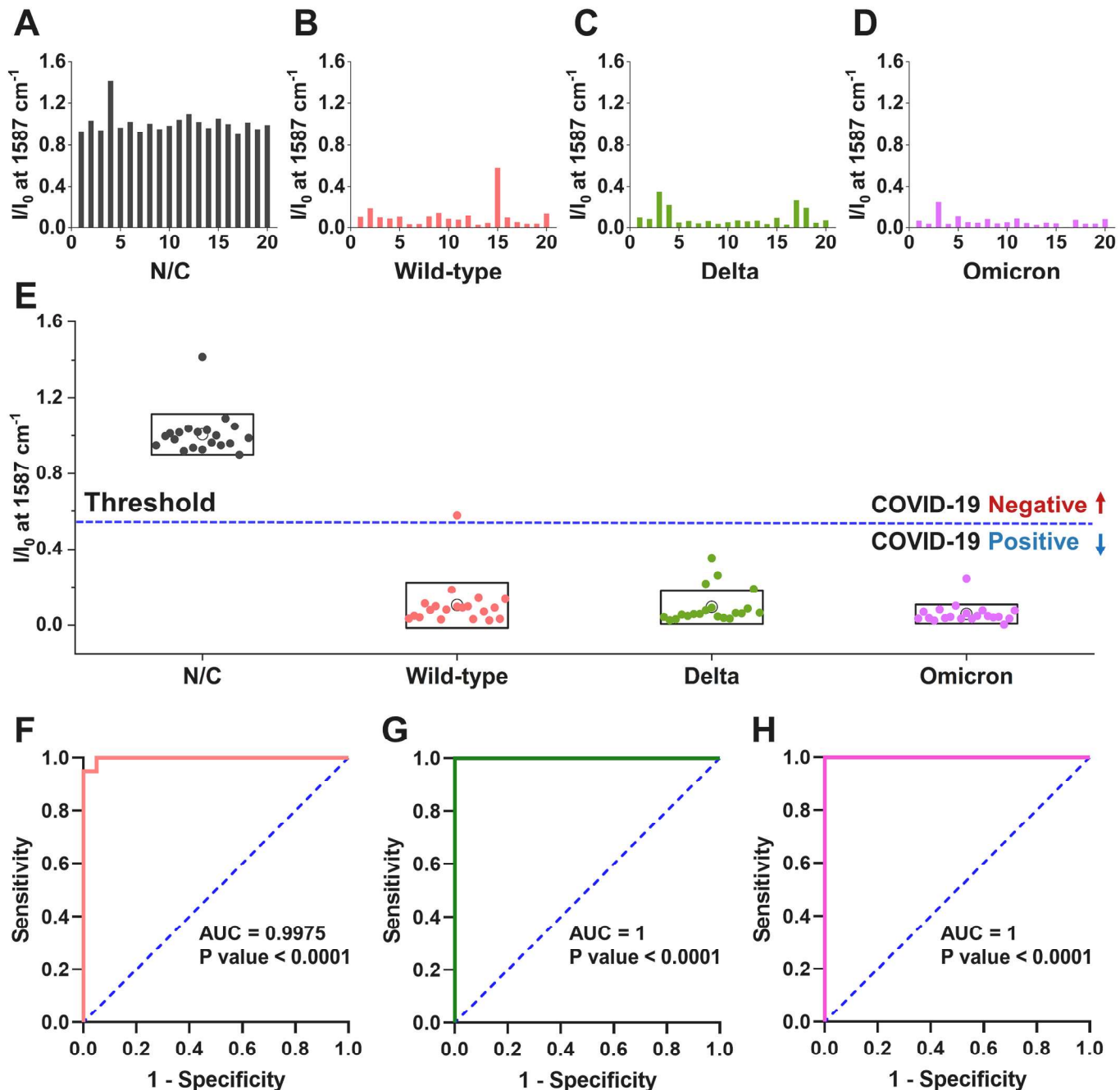

Fig. 5. Clinical validation of our SERS-based aptasensor. (A–D) SARS-CoV-2 detection in 80 nasopharyngeal specimens representing (A) negative controls or patients with (B) wild-type, (C) Delta, and (D) Omicron variants of SARS-CoV-2. (E) Sensitivity and specificity of detection of SARS-CoV-2 variants based on a threshold (dashed lines) calculated from the receiver operating characteristic (ROC) curve. The box indicates the standard deviation, and the white circle indicates the mean value. (F–H) ROC curves of diagnosis for (F) wild-type, (G) Delta, and (H) Omicron variants of SARS-CoV-2.

(AUC) was determined to be 0.9975, 1, and 1 for the WT, Delta, and Omicron variants, respectively, confirming the excellent accuracy for broad detection of SARS-CoV-2 (Fig. 5F–H).

Even though our aptamers were derived from an S protein from an early lineage of SARS-CoV-2 in 2020 (NCBI Reference Sequence: YP_009724390.1) (Wu et al., 2020), SpS1-C4 showed robust binding to the highly-mutated Delta and Omicron variants as well. Our aptamers bind to S1, which in turn recognizes the host-cell ACE2 receptor, and the results here indicate that this binding site may be especially well conserved across SARS-CoV-2 variants. Further studies will be required to clarify this, but our current results indicate that our platform could prove broadly applicable for detecting future variants of concern as well.

4. Conclusions

Timely diagnosis of SARS-CoV-2 is crucial to prevent the spread of the virus, particularly given the potential for emergence of new variants of concern that may elude existing diagnostic assays. Here, we report a label-free SERS-based aptasensor platform that combines a novel aptamer and silver nanoforest substrate to achieve ultra-sensitive, highly accurate detection of multiple SARS-CoV-2 variants. Using the particle display technique, we successfully isolated two DNA aptamers that exhibited a low nanomolar Kd for the viral S protein—to the best of our knowledge, this represents the highest-affinity aptamer reported to date for this target. We subsequently incorporated these aptamers into our label-free SERS-based aptasensor platform, achieving an attomolar detection limit for recombinant S protein. We then clinically validated our aptasensor platform with 60 clinical samples with SARS-CoV-2 (wild-type, Delta, and Omicron) and 20 negative controls, achieving excellent accuracy with high sensitivity and specificity for broad detection of SARS-CoV-2. This aptasensor has the potential to detect future variants of this virus, and the same design could be exploited to achieve rapid and economical development of diagnostic tools for a diverse range of other pathogens as well.

CRediT authorship contribution statement

Ki Sung Park: Conceptualization, Data curation, Formal analysis, Investigation, Writing – original draft. **Anna Choi:** Formal analysis, Investigation. **Hyun Jung Kim:** Formal analysis, Investigation. **Insu Park:** Formal analysis, Investigation. **Mi-Suk Eom:** Resources, SARS-CoV-2 clinical samples. **Sang-Gu Yeo:** Resources, SARS-CoV-2 clinical samples. **Ryeo Gang Son:** Formal analysis, Investigation. **Tae-In Park:** Formal analysis, Investigation. **Gyudo Lee:** Formal analysis, Investigation. **Hyongsok Tom Soh:** Conceptualization, Writing – review & editing. **Yoochan Hong:** Project administration, Data curation, Formal analysis, Writing – review & editing. **Seung Pil Pack:** Project administration, Data curation, Formal analysis, Writing – review & editing, All the authors discussed and approved the manuscript.

Declaration of competing interest

The authors declare that they have no known competing financial interests or personal relationships that could have appeared to influence the work reported in this paper.

Data availability

Data will be made available on request.

Acknowledgments

Appendix A. Supplementary data

Supplementary data to this article can be found online at https://doi.org/10.1016/j.bios.2023.115202.

References

Abdelhamid, M.A., Son, R.G., Park, K.S., Pack, S.P., 2022. Colloids Surf., B 219, 112830.
Adamson, B., Sikka, R., Wyllie, A., Premsrirut, P., 2022. Medrxiv 5. Preprint posted online, 2022-01. https://doi.org/10.1101/2022.01.04.22268770.
Ahmad, K.M., Oh, S.S., Kim, S., McClellen, F.M., Xiao, Y., Soh, H.T., 2011. PLoS One 6 (11), e27051.
Ambartsumyan, O., Gribanyov, D., Kukushkin, V., Kopylov, A., Zavyalova, E., 2020. Int. J. Mol. Sci. 21 (9), 3373.
Banerji, A., Wickner, P.G., Saff, R., Stone Jr., C.A., Robinson, L.B., Long, A.A., Wolfson, A.R., Williams, P., Khan, D.A., Phillips, E., 2021. J. Allergy Clin. Immunol. Pract. 9 (4), 1423–1437.
Barhoumi, A., Halas, N.J., 2010. J. Am. Chem. Soc. 132 (37), 12792–12793.
Broughton, J.P., Deng, X., Yu, G., Fasching, C.L., Singh, J., Streithorst, J., Granados, A., Sotomayor-Gonzalez, A., Zorn, K., Gopez, A., 2020. Nature biotechnology 38 (7), 870–874. MedRxiv. https://doi.org/10.1038/s41587-020-0513-4.
Chen, A., Yang, S., 2015. Biosens. Bioelectron. 71, 230–242.
Corman, V.M., Landt, O., Kaiser, M., Molenkamp, R., Meijer, A., Chu, D.K., Bleicker, T., Brünink, S., Schneider, J., Schmidt, M.L., 2020. Euro Surveill. 25 (3), 2000045.
Diehl, F., Li, M., He, Y., Kinzler, K.W., Vogelstein, B., Dressman, D., 2006. Nat. Methods 3 (7), 551–559.
Dressman, D., Yan, H., Traverso, G., Kinzler, K.W., Vogelstein, B., 2003. Proc. Natl. Acad. Sci. U.S.A. 100 (15), 8817–8822.
Drolet, D.W., Moon-McDermott, L., Romig, T.S., 1996. Nat. Biotechnol. 14 (8), 1021–1025.
Ellington, A.D., Szostak, J.W., 1990. Nature 346 (6287), 818–822.
Emery, S.L., Erdman, D.D., Bowen, M.D., Newton, B.R., Winchell, J.M., Meyer, R.F., Tong, S., Cook, B.T., Holloway, B.P., McCaustland, K.A., 2004. Emerg. Infect. Dis. 10 (2), 311.
Gans, J.S., Goldfarb, A., Agrawal, A.K., Sennik, S., Stein, J., Rosella, L., 2022. JAMA 327 (5), 485–486.
Gao, W., Li, B., Yao, R., Li, Z., Wang, X., Dong, X., Qu, H., Li, Q., Li, N., Chi, H., 2017. Anal. Chem. 89 (18), 9836–9842.
Gillibert, R., Triba, M.N., de la Chapelle, M.L., 2018. Analyst 143 (1), 339–345.
Hsieh, C.-L., Goldsmith, J.A., Schaub, J.M., DiVenere, A.M., Kuo, H.-C., Javanmardi, K., Le, K.C., Wrapp, D., Lee, A.G., Liu, Y., 2020. Science 369 (6510), 1501–1505.
Hu, P., Zhu, C., Jin, L., Dong, S., 2012. Biosens. Bioelectron. 34 (1), 83–87.
Hwang, M.T., Park, I., Heiranian, M., Taqieddin, A., You, S., Faramarzi, V., Pak, A.A., van der Zande, A.M., Aluru, N.R., Bashir, R., 2021. Adv. Mater. Technol. 6 (11), 2100712.
Jayasena, S.D., 1999. Clin. Chem. 45 (9), 1628–1650.
Kellner, M.J., Koob, J.G., Gootenberg, J.S., Abudayyeh, O.O., Zhang, F., 2019. Nat. Protoc. 14 (10), 2986–3012.
Kim, H.S., Lee, T., Yun, J., Lee, G., Hong, Y., 2021. Microchem. J. 160, 105632.
Li, Z., Yi, Y., Luo, X., Xiong, N., Liu, Y., Li, S., Sun, R., Wang, Y., Hu, B., Chen, W., 2020. J. Med. Virol. 92 (9), 1518–1524.
Moskovits, M., 1985. Rev. Mod. Phys. 57 (3), 783.
Pang, S., Labuza, T.P., He, L., 2014. Analyst 139 (8), 1895–1901.
Park, I., Lim, J., You, S., Hwang, M.T., Kwon, J., Koprowski, K., Kim, S., Heredia, J., Stewart de Ramirez, S.A., Valera, E., 2021. ACS Sens. 6 (12), 4461–4470.
Podder, S., Ghosh, A., Ghosh, T., 2021. J. Med. Virol. 93 (5), 2790–2798.
Scatena, E., Baiguera, S., Del Gaudio, C., 2019. Journal of Healthcare Engineering 2019, 2815789, 2019, 11 pages. https://doi.org/10.1155/2019/2815789.
Shao, K., Ding, W., Wang, F., Li, H., Ma, D., Wang, H., 2011. PLoS One 6 (9), e24910.
Simpson, S., Kaufmann, M.C., Glozman, V., Chakrabarti, A., 2020. Lancet Infect. Dis. 20 (5), e108–e115.
Spinelli, A., Pellino, G., 2020. Br. J. Surg. 107 (7), 785–787.
Taghdisi, S.M., Danesh, N.M., Beheshti, H.R., Ramezani, M., Abnous, K., 2016. Nanoscale 8 (6), 3439–3446.
Wang, J., Gong, Q., Maheshwari, N., Eisenstein, M., Arcila, M.L., Kosik, K.S., Soh, H.T., 2014. Angew. Chem. Int. Ed. 126 (19), 4896–4901.
Wu, F., Zhao, S., Yu, B., Chen, Y.-M., Wang, W., Song, Z.-G., Hu, Y., Tao, Z.-W., Tian, J.-H., Pei, Y.-Y., 2020. Nature 579 (7798), 265–269.
Yang, G., Li, Z., Mohammed, I., Zhao, L., Wei, W., Xiao, H., Guo, W., Zhao, Y., Qu, F., Huang, Y., 2021. Signal Transduct. Targeted Ther. 6 (1), 227.
Zhao, J., Pinchuk, A.O., McMahon, J.M., Li, S., Ausman, L.K., Atkinson, A.L., Schatz, G. C., 2008. Acc. Chem. Res. 41 (12), 1710–1720.
Zhou, J., Rossi, J., 2017. Nat. Rev. Drug Discov. 16 (3), 181–202.